Effects of individual and combined additions of transition elements (Zr, Ti and V) on the microstructure stability and elevated-temperature properties of Al-Cu 224 cast alloys

Peng Hu[1], Kun Liu[1,*], Lei Pan[2] and X.-Grant Chen[1,*]

[1] Department of Applied Science, University of Quebec at Chicoutimi, Saguenay (QC), Canada G7H 2B1

[2] Arvida Research and Development Centre, Rio Tinto Aluminum, Saguenay (QC), G7S 4K8, Canada

* Corresponding authors: kun.liu@uqac.ca (K. Liu), and xgrant_chen@uqac.ca (X.-G. Chen)

Abstract:

The effects of individual and combined additions of transition elements (TEs) Zr, Ti, and V on the microstructure evolution and elevated-temperature mechanical and creep properties of Al-Cu 224 cast alloys were investigated. All alloys had a mixed precipitate microstructure of θ″- and θ′-Al_2Cu after T7 heat treatment. During the thermal exposure at 300 ℃, θ″ transferred into θ′ as the predominant strengthening phase. The coarsening resistance of θ′ during the thermal exposure and further creep deformation was greatly improved by the addition of TEs. Individually, Zr addition demonstrated the best efficiency in stabilizing θ′, while the combination of Zr + V and Ti + Zr + V achieved the highest efficiency. The addition of TEs generally improved the yield strength (YS) at 300 ℃, and the ZrV and TiZrV alloys achieved the highest YS. A close correlation between the YS and the distribution and thermal stability of θ′ was observed. The creep resistance at elevated temperatures was affected by the thermal stability of θ′ and grain size. Zr-containing alloys (ZrV, Zr, and TiZrV) exhibit superior creep resistance. In terms of comprehensive properties, the combined addition of TiZrV alloy exhibited the best elevated-temperature performance.

Keywords: Al-Cu cast alloys; transition elements; precipitate coarsening; elevated-temperature mechanical properties; creep resistance.

1. Introduction

Owing to the increasing scarcity of nonrenewable resources and the need for environmental protection, improving engine efficiency and reducing fuel consumption have attracted widespread attention. Increasing the working temperature and power of the engine components is an effective approach [1]. Al–Cu cast alloys have attracted considerable interest for internal combustion engine applications owing to their light weight and superior mechanical performance [2, 3]. The room-temperature mechanical properties of Al-Cu alloys have been extensively studied. The typical precipitation sequence in Al-Cu alloys is given as follows: supersaturated solid solution (SSS) → GP I zones → GP II zones (θ″) → θ′ → θ [4, 5], where θ′ is found to be the main strengthening phase [6]. However, when the service temperature of engine components is above 200 ℃, the strengthening precipitates undergo coarsening rapidly, resulting in a significant softening of the alloys and causing severe failure during service [7, 8]. The high-temperature resistance of the materials is a crucial factor to take into account in order to fulfill the increasing demands for elevated-temperature applications.

Recent studies have revealed that the high-temperature properties of Al-Cu alloys can be significantly improved by microalloying with slow-diffusing transition elements (TEs) such as Sc, Zr, Ti, V, and Mn [9-18]. It has been reported that the YS of the Al–Cu 206 alloy at 300 °C reached 105 MPa after thermal exposure at 300 °C with the addition of Mn, Zr, and Ni [9]. In our recent works [10, 11], the elevated-temperature mechanical and creep properties at 300 °C of Al–Cu 224 type alloys could be further improved after exposure at 300 °C for 100 h via microalloying with Mg, Zr, V, and Ti. The improved elevated-temperature properties of Al-Cu alloys are primarily due to the enhancement of the thermal stability of the main strengthening phase of nanoscale θ′-Al_2Cu [9, 10, 12]. Several studies have demonstrated that the thermal stability of θ′ in Al-Cu alloys is promoted by the segregation of solute atoms of TEs at the Al/θ′ interface to inhibit the coarsening of θ′, such as Sc segregation [12-16], Ti segregation [17, 18], Zr segregation [3, 9, 18], V segregation [17], and Mn segregation [3, 9, 18]. Recently, the synergistic stabilizing role of TEs in Al-Cu alloys has drawn much attention. Jonathan et al. [17] reported that the separate addition of Zr/Ti and Mn can improve the stability of Al-Cu alloys at 200 ℃ and 300 ℃, respectively. Furthermore, Shyam et al. [18] demonstrated that the combined addition of Mn and Zr in Al-Cu alloys (termed ACMZ alloys) could further increase their thermal stability up to 350 ℃. They reported that Mn addition could segregate quickly to Al/θ′ interfaces and stabilize θ′ long enough

to allow other slower diffusion TEs (e.g., Ti and Zr) to segregate to Al/θ′ interfaces, thereby providing further protection [9, 18, 19]. The enhanced coarsening resistance of θ′ in ACMZ alloy also increases its creep resistance at 300 °C [20, 21]. However, the addition of TEs could result in the formation of thermally stable Al_3M dispersoids (M = Sc, Zr, Ti, V, etc.) in the aluminum matrix [13, 14, 22, 23], providing complementary strengthening at elevated temperatures [19, 22, 24]. In addition, these Al_3M dispersoids can provide heterogeneous nucleation sites for θ′ and retard the coarsening of θ′ precipitates [25].

Despite several studies on the high-temperature properties of Al-Cu alloys, there is still a lack of systematic investigation of the impact of individual and combined additions of TEs in the literature. In the present work, we designed eight Al-Cu alloys and focused on the different combinations of the three commonly used TEs in aluminum alloys (Zr, Ti, and V) to study their role in elevated-temperature mechanical and creep properties. The microstructural stability during current exposure and creep deformation were investigated using transmission electron microscopy. The compressive yield strength tests and creep tests at 300 °C were performed to compare the elevated-temperature properties with the different TEs additions.

2. Experimental procedures

Eight Al-Cu 224 alloys with a fixed amount of Mn (0.35 wt. %) but different combinations of Zr, Ti, and V additions were prepared, including the base alloy, three alloys with individual additions, three alloys with binary combinations, and one alloy with the ternary combination. The alloys were melted in a 300-kg electric resistance furnace. After reaching 750 °C, the melt was degassed with pure Ar for 10 min. All alloys were grain-refined with 0.05 wt. % Ti of the Al-5Ti-1B master alloy and cast in a permanent wedge mold preheated at 250 °C. The pouring temperature was 720 °C. The chemical compositions of the alloys analyzed using optical emission spectroscopy are listed in Table 1. All tested samples were cut from the same location as the wedge castings, as shown in the shaded part of Fig. 1a. All cast samples were initially subjected to the traditional T7 heat treatment (solution treatment at 495 °C/2 h + 528 °C/10 h; aging at 200 °C/4 h), after which an additional thermal exposure at 300 °C for 100 h was carried out to stabilize the microstructure, known as the T7A treatment. The details of the heat treatment procedure are shown in Fig. 1b.

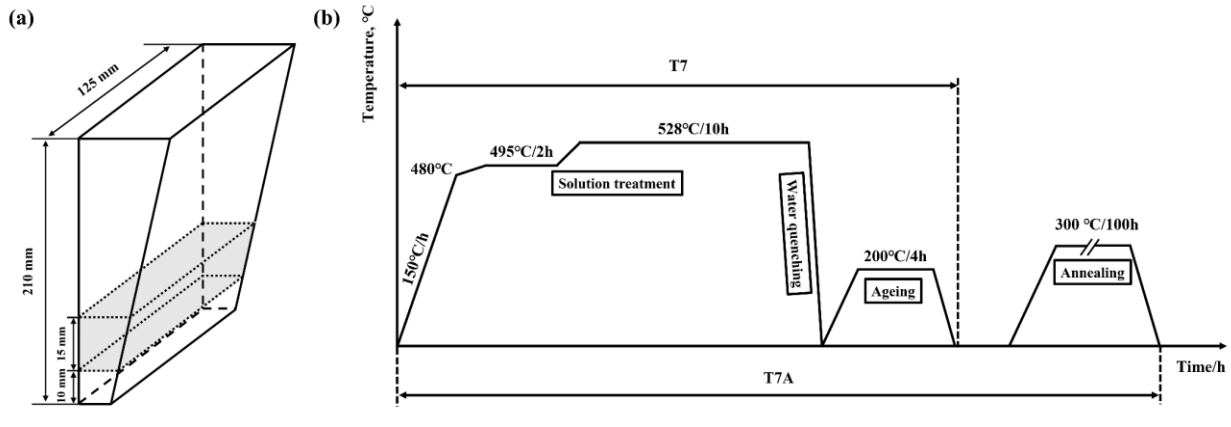

Fig. 1 The schematic graph of (a) the wedge casting and the location of sampling and (b) the heat treatment procedure applied in the present work.

Table 1 Chemical compositions of experimental alloys (wt.%).

Alloys	Si	Fe	Cu	Mn	Mg	Ti	V	Zr	Al
Base	0.06	0.12	4.70	0.35	0.14	0.05	0.01	0.01	Bal.
Zr	0.06	0.12	4.66	0.35	0.14	0.06	0.01	**0.15**	Bal.
Ti	0.09	0.10	4.62	0.34	0.12	**0.17**	0.01	0.01	Bal.
V	0.08	0.08	4.60	0.34	0.10	0.04	**0.23**	0.01	Bal.
ZrV	0.06	0.12	4.79	0.35	0.13	0.06	**0.17**	**0.15**	Bal.
TiZr	0.09	0.09	4.57	0.34	0.11	**0.18**	0.01	**0.16**	Bal.
TiV	0.08	0.08	4.65	0.34	0.16	**0.16**	**0.23**	0.01	Bal.
TiZrV	0.04	0.11	4.69	0.34	0.12	**0.17**	**0.21**	**0.15**	Bal.

The compressive tests at room temperature and 300 °C were conducted in a Gleeble 3800 thermomechanical simulator unit with a fixed strain rate of 10^{-3} s^{-1}. The 0.2% offset yield strengths were determined from the stress-strain curves. Cylindrical specimens with a diameter of 10 mm and a length of 15 mm were machined for compressive and creep tests. At least three samples were tested for each condition, and their average values were obtained. The compressive creep tests were performed on the T7A-treated samples at a fixed temperature of 300 °C for 100 h. The applied stress varied from 45 to 60 MPa.

The microstructures of all the alloys were observed using optical microscopy (OM) and transmission electron microscopy (TEM). The as-cast grain structure was revealed using Keller's reagent and quantified using ImageJ software, and at least 500 grains were measured to obtain the average grain size. A TEM study was carried out to characterize the precipitates after the T7, T7A,

and creep tests. The obtained TEM images were analyzed using the ImageJ software to quantify the parameters of the precipitates (thickness, length, and number density). At least 1000 precipitates were quantified for each alloy and condition. Details of the quantification method can be found in [8, 26, 27].

3. Results

3.1 As-cast and heat-treated microstructures

Fig. 2 shows the as-cast grain structures of the experimental alloys. Equiaxed grains were observed in all alloys, but the grain size varied with the addition of TEs. The measured grain sizes of all the alloys are summarized in Table 2. Based on the average grain size, the experimental alloys were divided into three groups: fine-grained (TiZr and TiZrV alloys), medium-grained (Ti, V, and TiV alloys), and coarse-grained (base, Zr, and ZrV alloys). The addition of Ti and V acted as grain growth restrictors and refined the grain structure [28]. As shown in Table 2, the grain sizes of all Ti/V-containing alloys were finer than those of the base alloy. For instance, the grain size decreased from 99 μm in the base alloy to approximately 60 μm in the Ti, V, and TiV alloys. Compared to Ti/V-containing alloys, the addition of Zr, especially the combination of Zr and V, poisoned grain refining [29, 30], leading to a much coarser grain structure in the Zr alloy (124 μm) and ZrV alloy (194 μm). Further additions of Ti to Zr-containing alloys can compensate for the Zr poisoning effect and effectively refine the grain structure. The finest grain structures were observed in TiZr (30 μm) and TiZrV (39 μm) alloys.

Typical microstructures in the as-cast and T7-treated conditions, as an example of three alloys (the base, TiZr, and TiZrV alloys), are shown in Fig. 3. The intermetallics in Fig. 3 were mainly identified according to their morphology, the results of SEM-EDS and the information in the literature [10, 11, 26]. In the as-cast condition (Figs. 3a–c), all experimental alloys consisted of α-Al dendrite cells/grains, θ-Al_2Cu, and Al_7Cu_2(Fe, Mn) intermetallics distributed along the cell/grain boundaries. In addition, a very small amount of primary Al_3M particles (M = Zr, Ti, and V or their combination) was found in the TEs-containing alloys (Figs. 3b and c), and they were distributed randomly in the matrix. After T7 heat treatment, most of the θ-Al_2Cu phase dissolved into the matrix (Figs. 3d–f), while Al_7Cu_2(Fe, Mn) and Al_3M barely changed (Figs. 3e and f). The thermal exposure at 300 ℃ for 100 h (T7A) did not affect the intermetallic Al_7Cu_2(Fe, Mn) or

Al_3M particles. No obvious difference in the optical microstructure was observed between the T7 and T7A conditions; hence, the microstructure images in the T7A condition are not shown here.

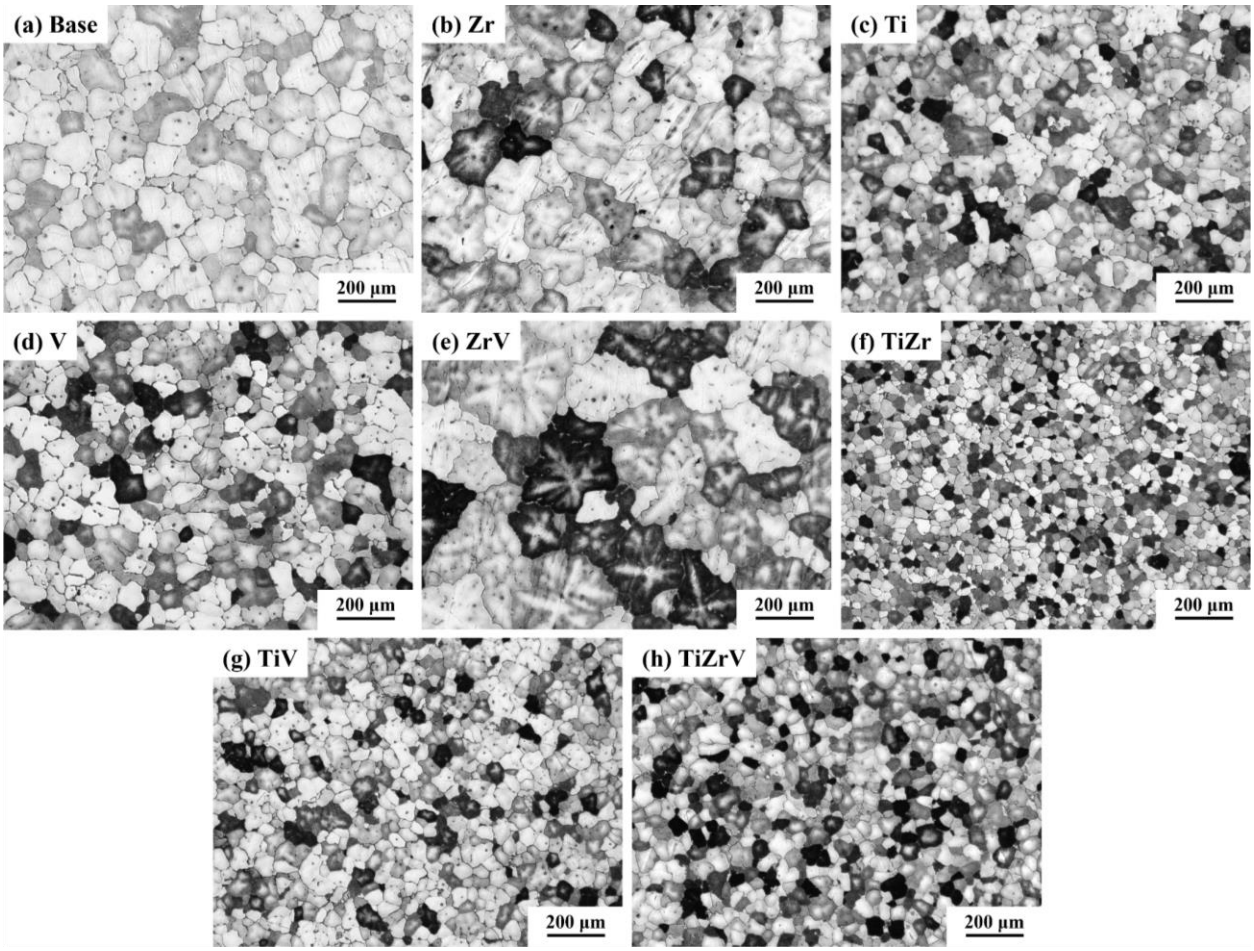

Fig. 2 The as-cast grain structures of the experimental alloys.

Table 2 The average grain sizes of the experimental alloys.

	Fine grain		Medium grain			Coarse grain		
Alloys	TiZr	TiZrV	Ti	TiV	V	Base	Zr	ZrV
Grain size, μm	30±3	39±4	54±9	54±8	66±11	99±22	124±22	194±46

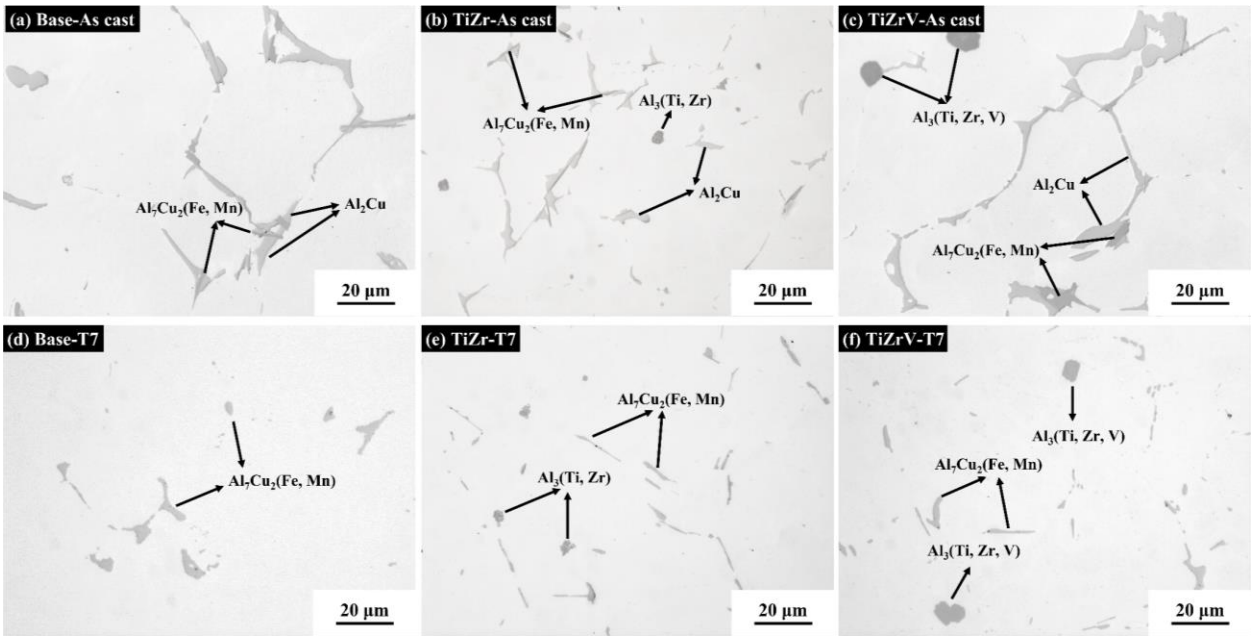

Fig. 3 The OM microstructure images of three alloys at as-cast and T7 conditions.

The bright-field TEM images viewed along the $<001>_{\alpha\text{-Al}}$ direction of all the experimental alloys after T7 treatment are shown in Fig. 4. Two types of disk-shaped θ″ and θ′ were observed, as confirmed by the selected area diffraction patterns (SADP) shown in Fig. 4(i). The size of θ″ precipitates was much smaller than that of θ′. A mixture of θ″ and θ′ in the aluminum matrix was found in the base alloy and in most Zr-containing alloys, including Zr, ZrV, and TiZrV alloys (Figs. 4a, b, e, and h). However, the microstructure was dominated by θ′ precipitates in the Ti/V-containing alloys, namely the V, Ti, TiZr, and TiV alloys (Figs. 4c, d, f, and g). A few θ″ precipitates are observed as minor phases. This may be due to the different solute-vacancy binding energies of TEs, which can affect the diffusion of Cu atoms [31-33]. The mechanism needs further exploration. A non-uniform distribution of precipitates is often observed in the second group of alloys. For instance, most θ″ precipitates were found near the grain boundaries, probably owing to the segregation of the TEs and Cu [33, 34], whereas the predominant precipitates turned into θ′ as the distance from the grain boundaries increased (Fig. 5).

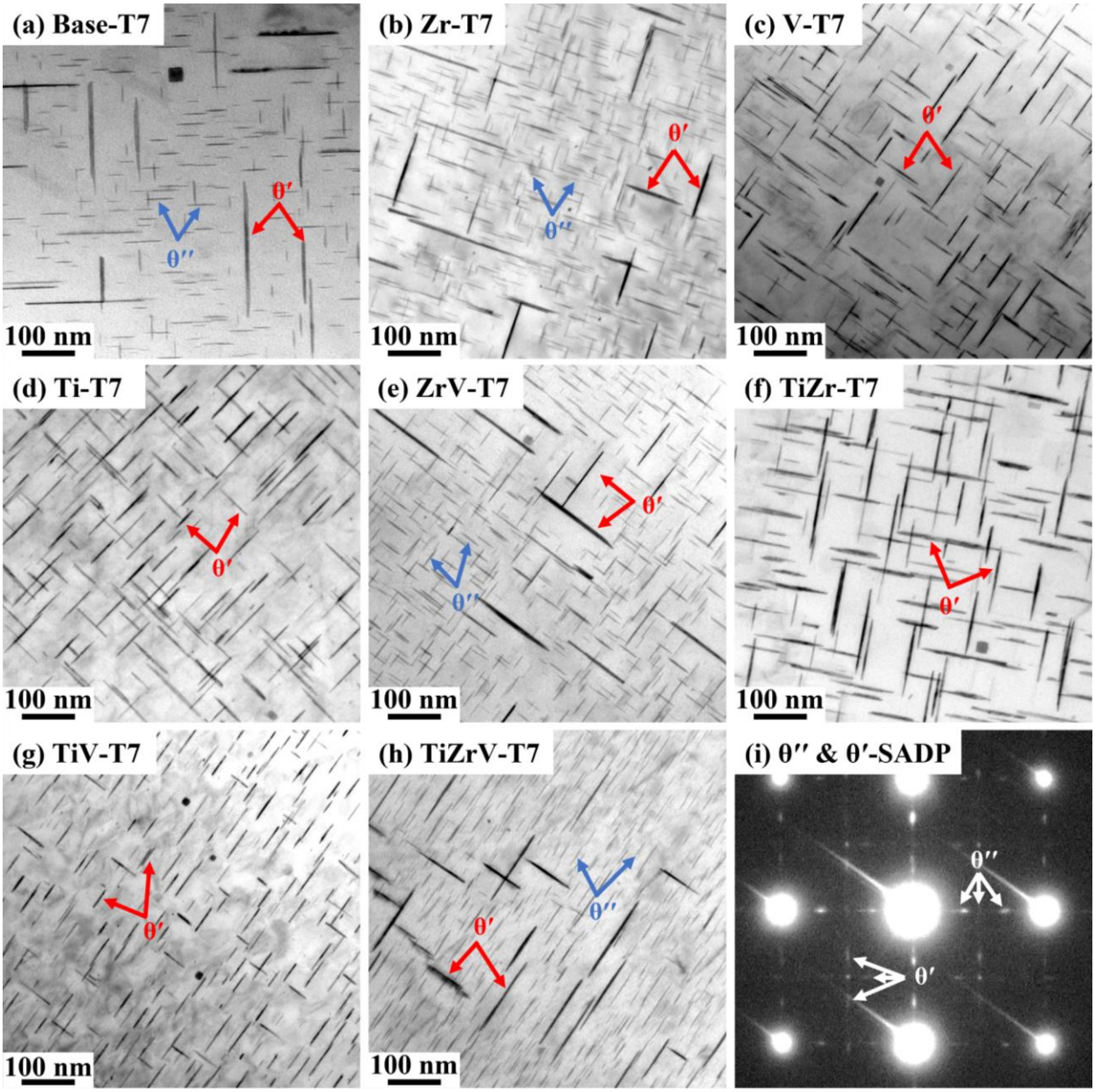

Fig. 4 Bright-field TEM images viewed along <001>$_{\alpha\text{-Al}}$ showing the precipitate microstructures of the experimental alloys after T7 treatment (a-h) and (i) typical SADP.

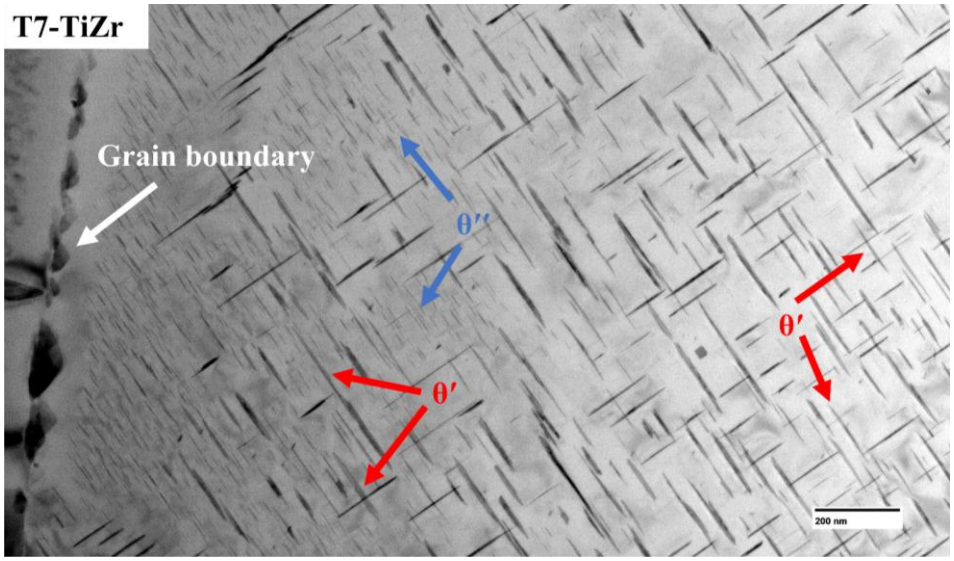

Fig. 5 Bright-field TEM images viewed along <001>$_{\alpha\text{-Al}}$ showing a non-uniform distribution of θ″ and θ′ precipitates in the TiZr alloy after T7.

After thermal exposure at 300 ℃ for 100 h to stabilize the microstructure (T7A), θ′ precipitates became the predominant strengthening phase in all the experimental alloys, as shown in the TEM images in Fig. 6. During thermal holding at 300 ℃, the θ″ phase was not stable at 300 ℃ and either dissolved into the matrix or transferred into θ′ [10, 35], and then θ′ underwent a coarsening process with increased holding time. The finer the size and the higher the number density of θ′ after thermal exposure, the more thermally stable is the microstructure. The θ′ characteristics after T7A were quantified, and the results are presented in Table 3. In general, TEs-containing alloys refined θ′, exhibiting a smaller size (in terms of both length and thickness) and a higher number density than those of the base alloy. When the TEs were added individually, the length of θ′ in the Ti, Zr, and V alloys (150-160 nm) was ~10% shorter than that of the base alloy (171 nm), while the number density was 1.5 to 2 times higher. Among the three individually added alloys, the Zr alloy exhibited the finest distribution of θ′, and thus it was the most effective at stabilizing the θ′ precipitates. In the case of the combination of TEs, the distribution of θ′ was further improved in the ZrV and TiZrV alloys. For instance, the number density of θ′ was increased from 2.5×10^{-7} (Zr alloy) to 2.7×10^{-7} (TiZrV alloy) and further to 3.2×10^{-7} (ZrV alloy), while the length and thickness of θ′ were in the same range in all three alloys. Based on the quantitative results (Table 3), the thermal stabilities of the θ′ precipitates in the eight experimental alloys were distinct in the following sequence:

ZrV alloy > TiZrV alloy > Zr alloy ≈ TiZr alloy > TiV alloy ≈ Ti alloy ≈ V alloy > base alloy.

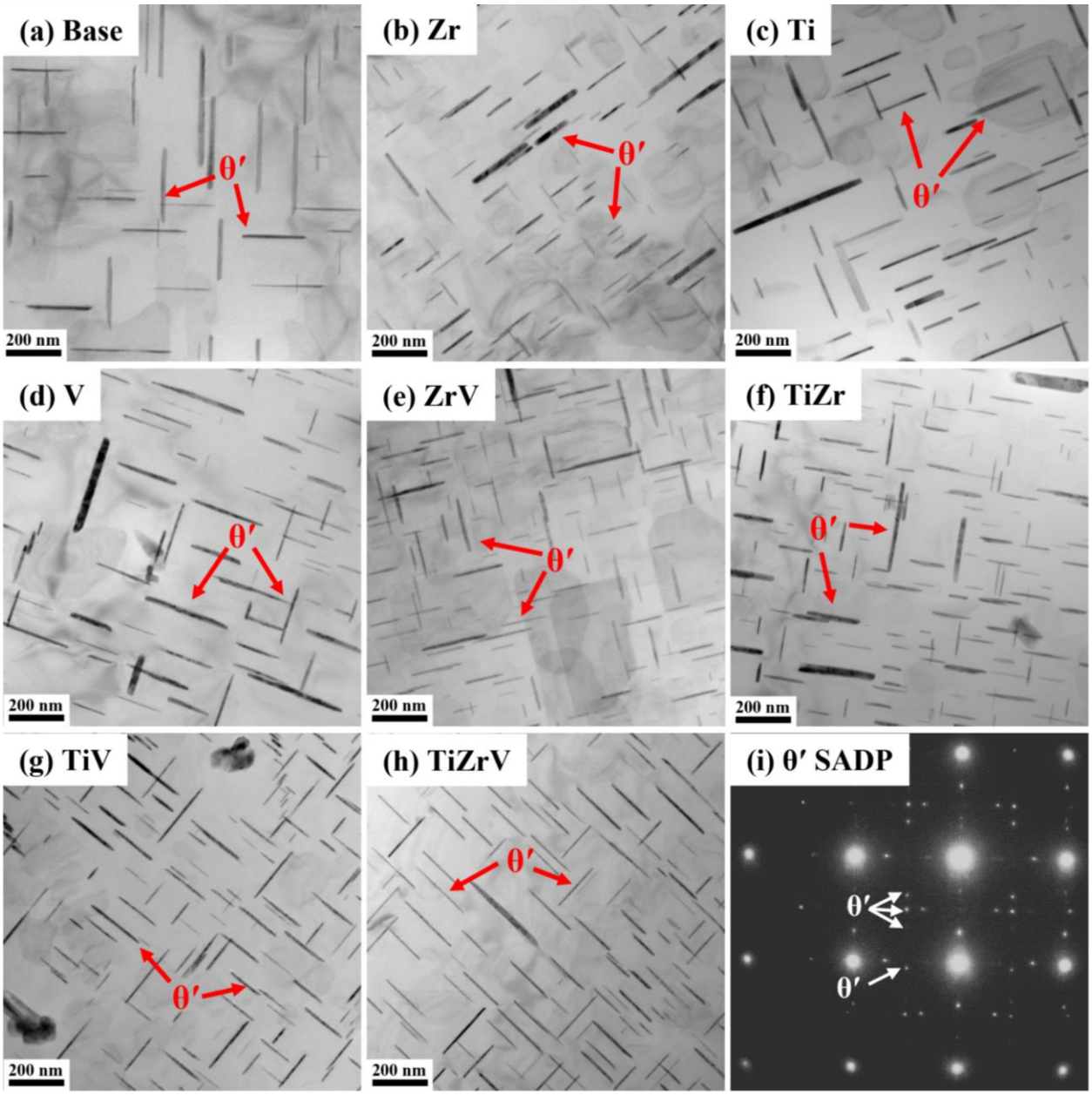

Fig. 6 Bright-field TEM images viewed along <001>$_{\alpha\text{-Al}}$ showing the θ′ precipitates of the experimental alloys after T7A treatment (a-h) and (i) typical SADP of θ′.

3.2 Mechanical properties

The compressive YS of all the experimental alloys after T7A at room temperature and 300 ℃ are shown in Fig. 7. The results revealed that all the TEs-containing alloys exhibited higher YS at both room temperature and 300 ℃ relative to the base alloy, but the enhancement of YS varied

from one alloy to another. Zr addition was more effective than Ti or V addition when added individually. As shown in Fig. 4, the YS at 300 ℃ of the Zr alloy reached 113 MPa, an increase of 17.7% compared to the base alloy. However, the enhancements provided by Ti and V alloys were 7.3%. The performance of the combination of TEs also changed significantly. For example, the YS at 300 ℃ was significantly improved by the combination of Zr + V and Ti + Zr+ V, and it was higher than 130 MPa, with an increase of >35% compared to the base alloy. On the other hand, the elevated temperature YS of the TiV alloy was the same as that of the Ti and V alloys, whereas the TiZr alloy had a moderate increase in YS (14.5%) relative to the base alloy. The change in the YS at room temperature followed the same trend as at 300 ℃. In brief, the impact of the individual and combined additions of TEs on the elevated-temperature YS of the experimental alloys is as follows:

ZrV alloy ≈ TiZrV alloy > Zr alloy ≈ TiZr alloy > TiV alloy ≈ Ti alloy ≈ V alloy > base alloy.

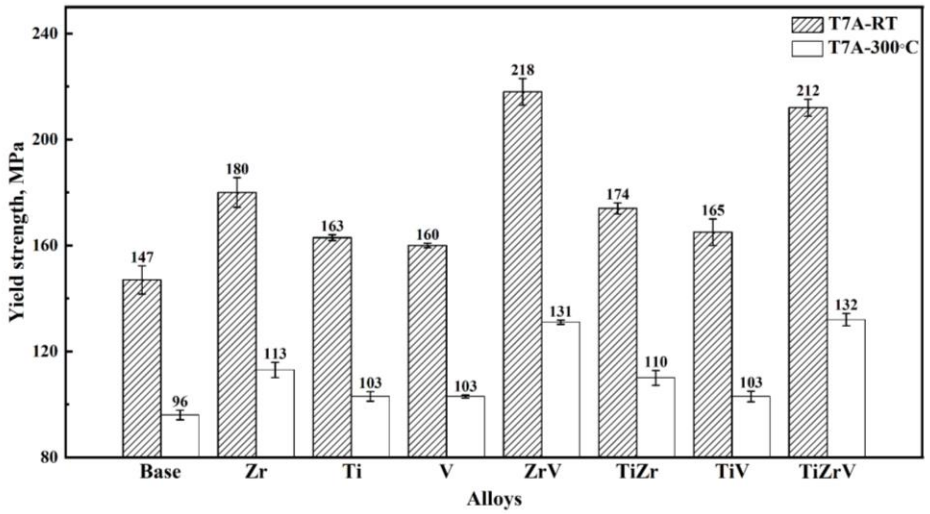

Fig. 7 The compressive YS of different TEs-containing alloys at room temperature and 300 ℃ in the T7A state.

3.3 Creep behavior

Fig. 8 shows the typical compressive creep curves and corresponding creep rate curves tested at 300 ℃ for 100 h on the T7A samples at 50 MPa and 60 MPa. At low applied stresses (45-50 MPa), all alloys displayed two creep stages: the primary stage and the secondary (quasi-steady) stage. At the beginning of creep (primary stage), the creep strain increased sharply owing to work

hardening, but the creep rate decreased with time. With further creep deformation, the strain increased constantly, and the creep rate reached its lowest value and remained almost stable at the quasi-steady stage because of the balance between work-hardening and dynamic softening. The quasi-steady stage took the most creep range, and the minimum creep rates were the average values measured from the quasi-steady stage. When the applied stress increased to a high level (55-60 MPa), most alloys still showed two typical creep stages, while the base and Ti alloys displayed a tertiary creep stage after the quasi-steady stage (Fig. 5b and d), in which the creep strain increased sharply and the creep rate was no longer constant. The occurrence of the tertiary creep stage indicates that such alloys lost their microstructural stability and started to fail during creep.

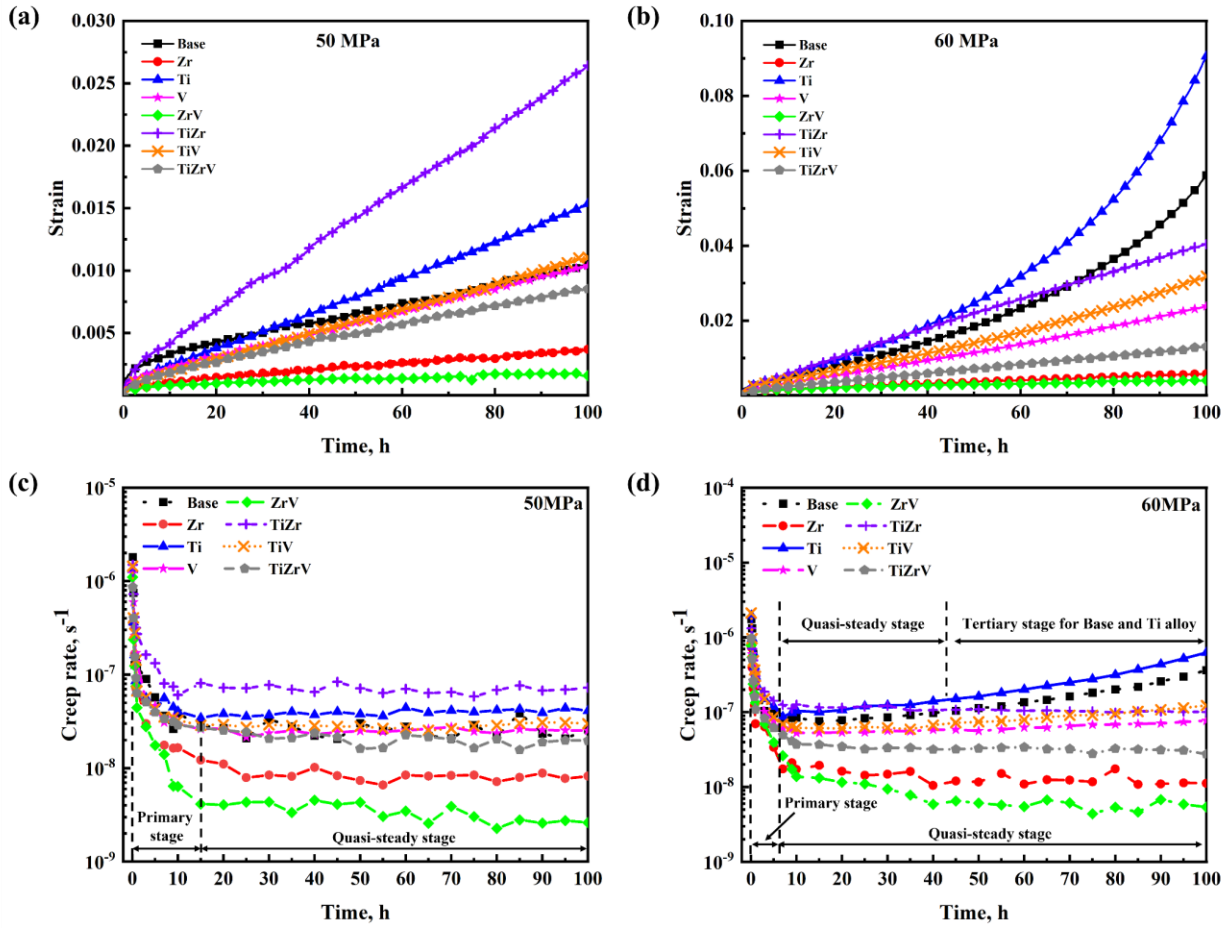

Fig. 8 Typical creep curves of the experimental alloys at (a) 50 MPa and (b) 60 MPa, and the creep rate curves at (c) 50 MPa and (d) 60 MPa.

The minimum creep rates and total strains as functions of applied stress are shown in Fig. 9. As shown in Fig. 9a, a linear fit was applied to obtain the stress exponents for each alloy. The

minimum creep rate, which is usually used to indicate the creep resistance, shows a large difference among the TE-containing alloys (Fig. 9a). Most Zr-containing alloys, such as Zr, ZrV, and TiZrV alloys, showed lower minimum creep rates compared to the base alloy, indicating enhanced creep resistance. The lowest minimum creep rate was observed for the ZrV alloy. In contrast, the minimum creep rate was higher in the Ti, TiV, V, and TiZr alloys than that in the base alloys. These alloys had a negative effect on the creep resistance. The total strain exhibited the same tendency as the minimum creep rate when the applied stress was less than 50 MPa (Fig. 9b). With a further increase in the applied stress, the base and Ti alloys underwent the tertiary creep stage, which led to a much higher total strain than that of the other alloys, indicating the poorest creep resistance. Based on the different creep behaviors shown in Figs. 8 and 9, the alloys can be divided into three groups: those with high creep resistance (ZrV, Zr, and TiZrV alloys), those with weak creep resistance (TiV, V, and TiZr alloys), and those with poor creep resistance (Ti and base alloys).

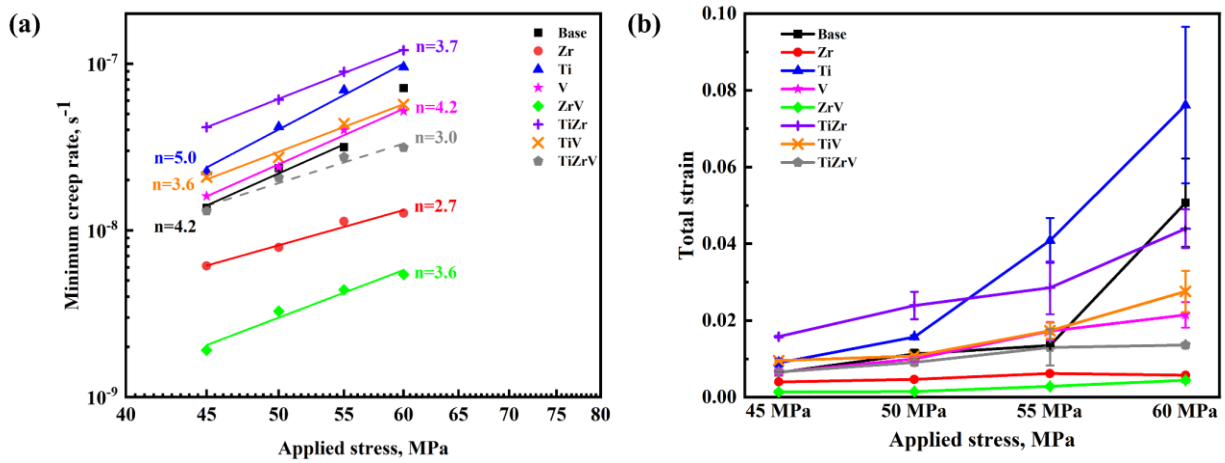

Fig. 9 (a) The minimum creep rate (logarithmic scale) and (b) the total strain as a function of applied stress after the creep tests at 300 ℃ for 100 h.

The relationship between the minimum creep rate and the applied stress can be described by the power-law equation as follows [36-38]:

$$\varepsilon = A\sigma^{n} \exp\left(\frac{-Q}{RT}\right) \quad (1)$$

where ε is the minimum creep rate, A is the material constant, σ is the applied stress, n is the stress exponent, Q is the apparent activation energy, T is the absolute temperature, and R is an ideal gas constant.

The values of n correspond to the well-developed creep mechanisms reported in references [26, 39-41]. If n=1, the creep deformation is believed to be dominated by diffusion creep; the value of n=2 is related to grain boundary sliding; and when n=3-6, the creep is mainly controlled by dislocation creep. The value of n in the present work varied from 3 to 5, as shown in Fig. 6(a); therefore, the creep process of 224 alloys under applied stresses (45-60 MPa) was believed to be dominated by dislocation creep.

3.4 Microstructure evolution during creep

During the creep tests, the T7A samples experienced not only further thermal exposure at 300 ℃ but also external stress. Typical TEM images after the 50 MPa creep tests are shown in Fig. 10. The selected diffraction patterns (not shown here) confirmed that the precipitates after the creep test were still θ′ in all experimental alloys. The θ′ characteristics of the creep samples are summarized in Table 3. Compared to θ′ before creep (Fig. 6 and Table 3), the θ′ precipitates after the creep test in all the alloys experienced further coarsening, became longer and thicker, and their number density decreased. In the base alloy, the length and thickness of θ′ increased by 10% and 12.5%, respectively, while the number density decreased by 37%. However, the TEs-containing alloys exhibited a much lower coarsening trend and an increase in the length and thickness of θ′, as well as a minor decrease in the number density. Among the TEs-containing alloys, the Zr-containing alloys (Zr, ZrV, and TiZrV alloys) still displayed higher coarsening resistance, as their number densities of θ′ were 45-70% higher than those of the Ti, V, and TiV alloys.

The interactions between θ′ precipitates and dislocations during creep were observed using TEM. Fig. 11 shows typical weak-beam dark-field TEM images for some TE-containing alloys under an applied stress of 50 MPa. Several dislocation segments climbed above the θ′ precipitates. This evidence confirms that the creep mechanism was dominated by dislocation creep in the present work, where the stress exponents of all the experimental alloys ranged between 3 and 5 (Fig. 6a).

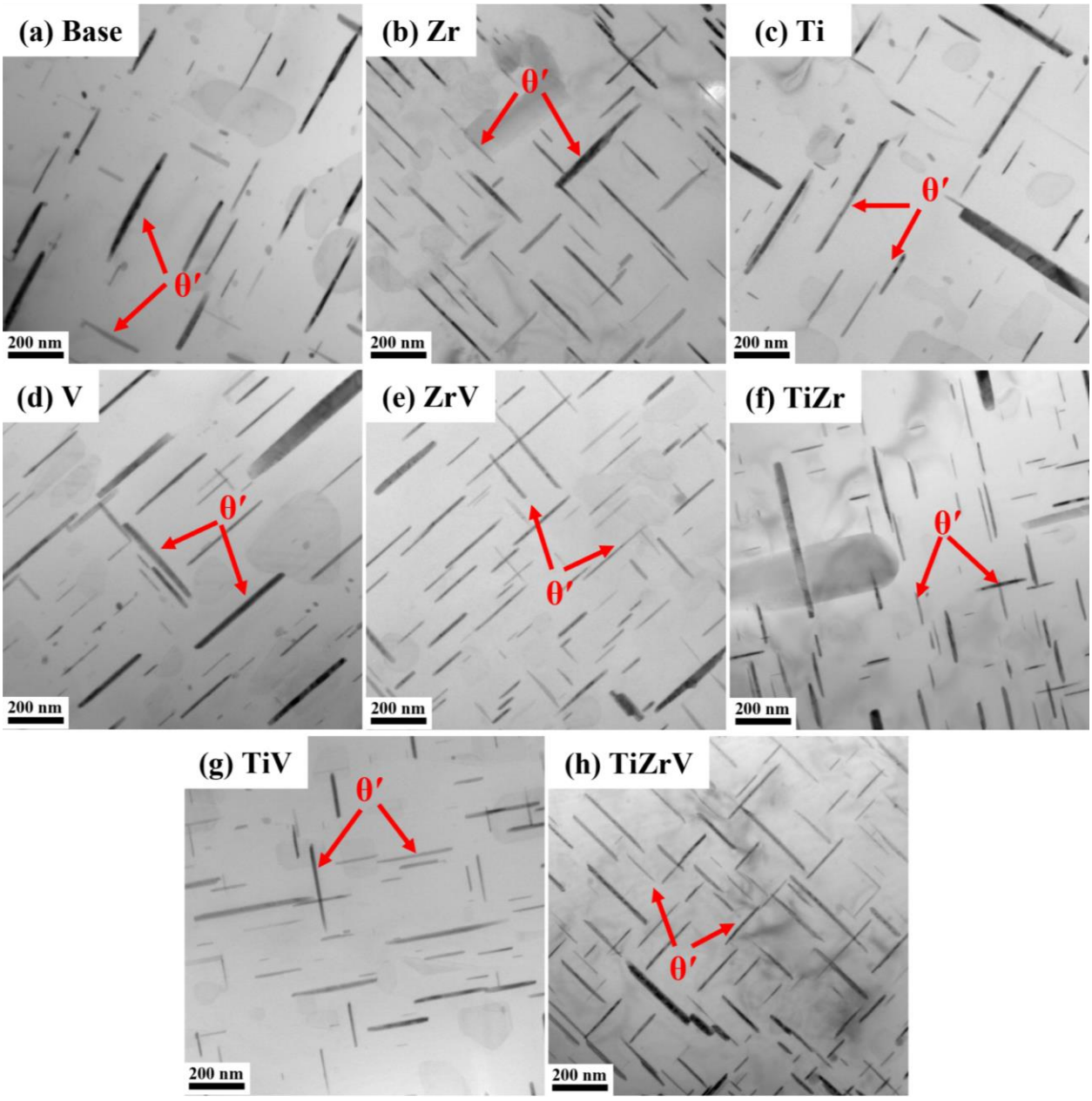

Fig. 10 Bright-field TEM images of the experimental alloys viewed along $<001>_{\alpha\text{-Al}}$ after 50 MPa creep tests.

Table 3 The quantitative TEM results of the θ′ in the experimental alloys after T7A and 50 MPa creep tests.

Alloys	State	Average length (nm)	Average thickness (nm)	Number density (nm^{-3})
Base	T7A	170.8	14.3	1.2×10^{-7}
	50 MPa Crept	187.9	16.1	7.6×10^{-8}
Zr	T7A	153.5	12.5	2.5×10^{-7}
	50 MPa Crept	166.4	13.9	1.6×10^{-7}
Ti	T7A	156.8	13.2	1.9×10^{-7}
	50 MPa Crept	174.7	14.1	1.1×10^{-7}
V	T7A	162.3	13.7	1.7×10^{-7}
	50 MPa Crept	175.3	14.6	1.1×10^{-7}
ZrV	T7A	146.8	11.7	3.2×10^{-7}
	50 MPa Crept	163.4	13.4	2.0×10^{-7}
TiZr	T7A	153.4	13.0	2.4×10^{-7}
	50 MPa Crept	164.8	13.7	1.5×10^{-7}
TiV	T7A	160.2	13.2	2.0×10^{-7}
	50 MPa Crept	168.6	14.3	1.2×10^{-7}
TiZrV	T7A	159.6	12.4	2.7×10^{-7}
	50 MPa Crept	164.7	13.5	1.8×10^{-7}

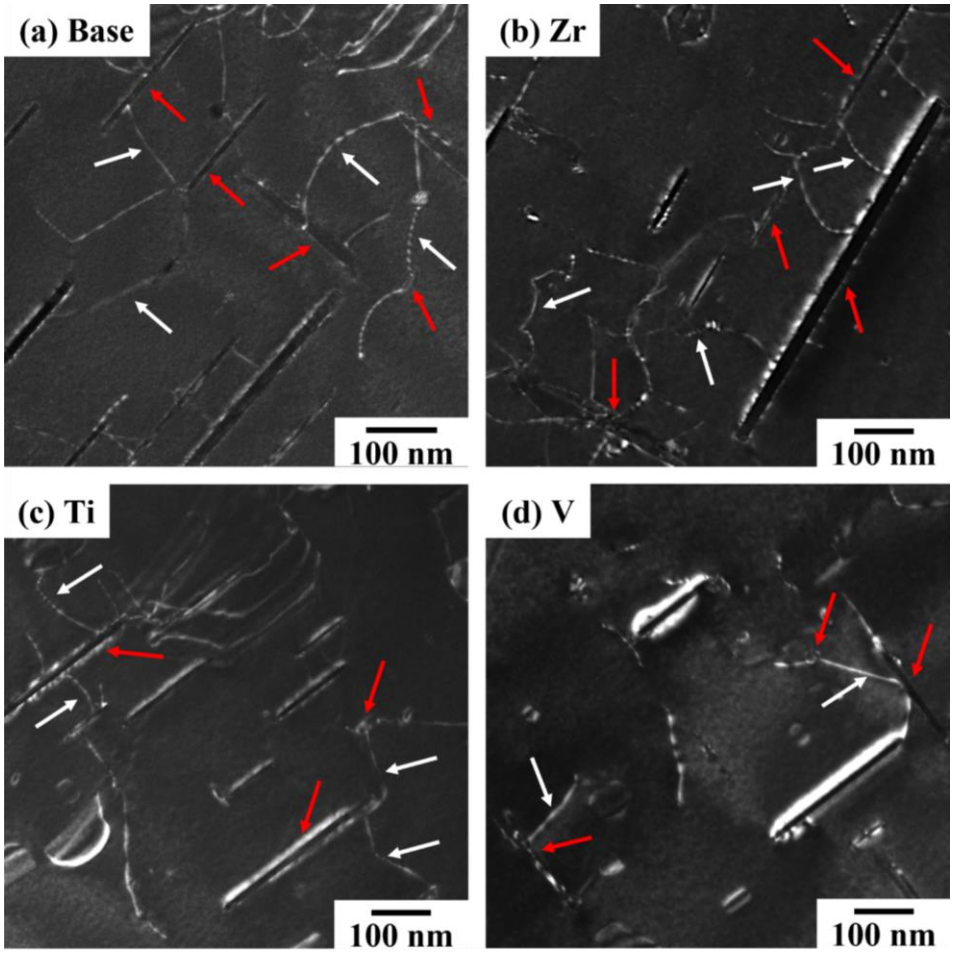

Fig. 11 Weak-beam TEM images of crept samples viewed along <001>$_{\alpha\text{-Al}}$ demonstrating the interaction between θ′ precipitates and dislocations. The dislocations and θ′ are marked by the white and red arrows, respectively.

4. Discussion

4.1 Effect of TEs on the thermal stability of precipitates and the YS

After the T7A treatment and creep test, only θ′ precipitates remained in the aluminum matrix as the strengthening phase (Figs. 6 and 10). To simplify the characteristics of θ′ and to better describe the θ′ stability, a widely used microstructural parameter λ, the effective planar interprecipitate spacing, was introduced, which is expressed in the following equation [8, 27, 33].

$$\lambda = 1.23\frac{1.030}{\sqrt{N_v d_t}} - \frac{\pi d_t}{8} - 1.061 t_t \quad (2)$$

where N_v, d_t and t_t are the number density, true length, and thickness of the precipitate, respectively.

The effective planar inter-precipitate spacing λ combines the number density, length, and thickness of precipitates to provide a simple and clear description of the distribution of θ′ and the coarsening resistance (thermal stability). The lower the value of λ, the finer the distribution, and the higher the thermal stability of the precipitates during thermal exposure and creep. The λ values of both the T7A-treated and 50 MPa-crept samples were calculated, and the results are shown in Fig. 12a. After 100 h of thermal exposure at 300 ℃ (T7A), the base alloy exhibited a very high value of λ, indicating the poor thermal stability of θ′. In general, a much lower λ value was found in the TEs-containing alloys, indicating the improved thermal stability of θ′. The sequence of the λ values from low to high in all the experimental alloys is as follows: ZrV, TiZrV, Zr, TiZr, TiV, Ti, V, and the base alloys. The results are consistent with the order of the thermal stability of the θ′ precipitates in the alloys as observed by TEM images and quantitative analysis (Fig. 6 and Table 3). Because of the further thermal exposure to external stress during the creep test, the θ′ in all the samples continued to coarsen. The λ values in the 50 MPa-crept samples were higher than those in the T7A samples (Fig. 12a). However, the tendency of the λ value change is nearly identical to that of the T7A state, and thus the thermal stability of θ′ in different alloys after creep tests is also identical to that in the T7A state.

Al-Cu 224 alloys are typical precipitation-strengthened alloys, and the difference in θ′ distribution (λ) yields different mechanical strengths. The sequence of the λ values is almost the same as the order of the YS in the T7A state (section 3.2, Fig. 10). The lower the interprecipitate spacing λ, the higher the elevated-temperature YS of the experimental alloy. As mentioned previously, the base alloy had a coarse precipitate distribution with the highest λ, resulting in the lowest YS at 300 ℃. The Zr-containing alloys generally exhibited a finer precipitate distribution with lower λ values, and hence had a higher YS than the Ti/V-containing alloys. Among all the experimental alloys, the ZrV and TiZrV alloys exhibited the lowest λ with the highest YS. With the simplified parameter λ, a close relationship between the YS and thermal stability of the precipitates was established with polynomial fitting and became easily recognizable (Fig. 12b), in which the elevated temperature YS depended on the distribution and thermal stability of the main strengthening phase of θ′.

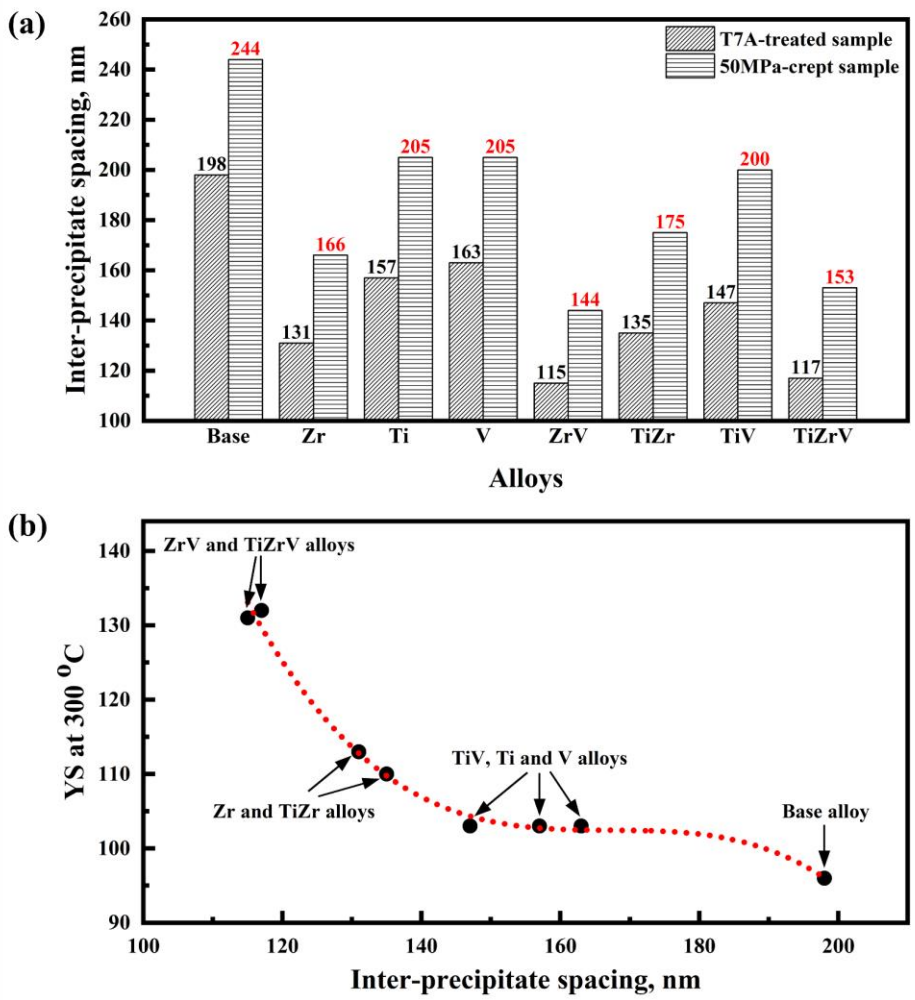

Fig. 12 (a) The inter-precipitate spacing of T7A-treated and 50MPa-crept samples and (b) the relationship between the λ and the YS at 300 ℃.

As reported in previous studies [9, 18, 25], there are two possible mechanisms by which the TEs can stabilize θ′. First, the solutes of the TEs diffuse and segregate to the Al/θ′ interfaces, inhibiting coarsening [9, 18]. Second, θ′ heterogeneously nucleated on the Al_3M dispersoids to form compact precipitates, which reduced the elastic strain energy and resulted in significantly delayed coarsening [25].

Because all alloys in this study contained a reasonable amount of Mn (0.35 wt. %), the discussion of the solute segregation includes the Mn and other TEs. During the thermal exposure at 300 ℃ (T7A), Mn diffused much faster and first segregated to the Al/θ′ interfaces because of its higher diffusion rate relative to the other Zr, Ti, and V. This builds the first barrier to retard the growth of θ′. However, this protection is quite weak, as shown for the base alloy. The further

stabilization of θ′ during thermal exposure mainly depends on the diffusion rates of Zr, Ti, and V in the aluminum matrix. It is reported that Zr diffuses more than 10 times faster than Ti and more than 1000 times faster than V in the Al matrix at 400 °C [19]. Hence, the efficiency of Zr in stabilizing θ′ was higher than that of Ti and V. A schematic illustration of how the TEs (Mn, Zr, Ti, and V) stabilize θ′ is shown in Fig. 13. In the base alloy, only Mn solutes segregated to the Al/θ′ interfaces (Fig. 13a), and the θ′ precipitates were not fully protected. In the presence of Zr solutes in the Zr alloy (Fig. 13b), Mn first segregates to Al/θ′ interfaces to build a first protective layer to allow the Zr solutes to diffuse and segregate to the Al/θ′ interfaces for further protection. The combination of Mn and Zr provides higher protection than the base alloy, resulting in a finer and denser distribution of θ′. For the Ti or V alloys, both solutes would spend a much longer time segregating to Al/θ′ interfaces owing to their lower diffusion rates. As a result, with the same time of thermal exposure, there would be less Ti and V solutes on the Al/θ′ interfaces (Fig. 13c), resulting in a coarser θ′ and a weaker thermal stability than the Zr alloy.

It is apparent that for combined additions, Zr-containing alloys would be superior to Ti- or V-containing alloys for building a protective layer in Al/θ′ interfaces. The λ values of the ZrV and TiZrV alloys were much lower than those of the TiV alloys. Within the Zr-containing alloys, the λ values of the combined additions (ZrV and TiZrV alloys) are also lower than that of the Zr addition alone (the Zr alloy). This is because the further addition of Ti and V can provide extra solute atoms in the Al/θ′ interfaces, which would form a denser protective layer in inhibiting θ′ coarsening during prolonged thermal exposure. Hence, the combinations of Zr + V and Ti+ Zr+ V are more effective in enhancing the thermal stability of Al-Cu alloy than the sole addition of Zr. The results also confirm the similar finding in our previous work [11]. This mechanism (Fig. 13) can provide a satisfactory explanation for the different coarsening resistances of the experimental alloys, as shown in Fig. 12a.

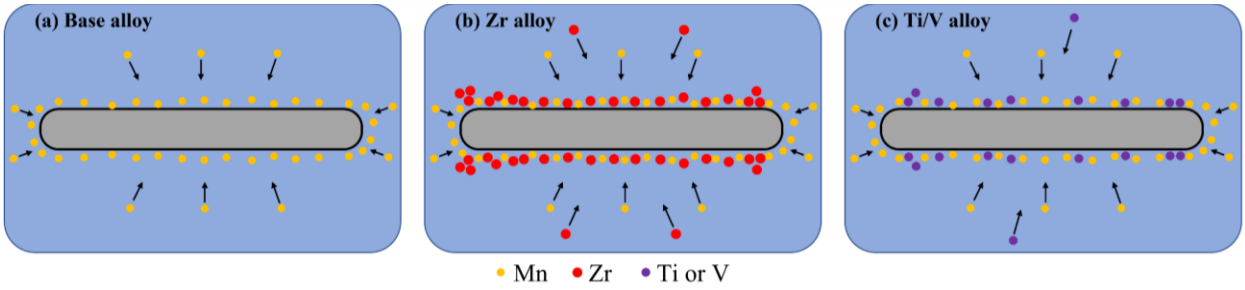

Fig. 13 Schematic illustration of the solute segregation in Al/θ′ interfaces to stabilize the θ′ (a) the base alloy only contained Mn, (b) Zr alloy with both Mn and Zr, and (c) the Ti or V alloy with the combination of Mn and Ti or Mn and V.

In the Zr-containing alloys, a reasonable number of Ll_2-Al_3Zr dispersoids were formed during the solution treatment (Fig. 14). During aging (T7), the pre-existing Al_3Zr dispersoids provided heterogeneous nucleation sites for θ′, resulting in the formation of compact θ′ precipitates to reduce the interfacial and strain energy [25], as shown in Fig. 14a. After further thermal exposure (T7A), the size of the compact θ′ with Al_3Zr was found to be smaller than that of the precipitates without Al_3Zr, as shown in Fig. 14b. A recent study [18] found that the microstructure with co-existence of θ′ and Ll_2-Al_3M was highly stable to inhibit the precipitate coarsening beyond 300 ℃ in Al-Cu alloys. This could be a complementary mechanism to explain the excellent thermal stability of the θ′ precipitates in Zr-containing alloys.

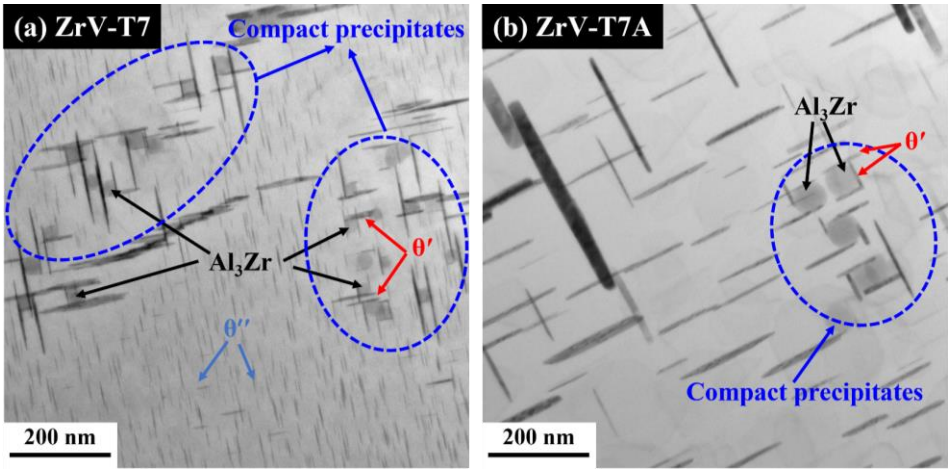

Fig. 14 (a) The nucleation and growth of θ′ on Al_3Zr to form compact precipitates during ageing (T7) and (b) the compact θ′ showing a smaller size after thermal exposure (T7A).

4.2 Effect of TEs on the creep resistance

The different TEs and their various combined additions exhibited different impacts on the creep resistance, as described in section 3.3 (Figs. 8 and 9). As the creep deformation was dominated by dislocation creep in all the alloys, the creep resistance was first influenced by the distribution and thermal stability of the θ′ precipitates (λ), which is closely related to the interaction with dislocations and their movement during creep deformation. Prior to the creep test, the base alloy possessed the highest λ, and dislocations moved easily in the Al matrix. In addition, θ′ in the crept sample of the base alloy was severely coarsened, with the highest λ after creep (Figs. 10a and 12a). The alloy displayed the diminished hindering effect on dislocation movement, causing a short secondary stage and the occurrence of the unstable "ternary stage" and leading to the poorest creep resistance. The Zr-containing alloys (ZrV, Zr, and TiZrV) displayed very low λ values before and after creep, provided a stronger hindering effect on dislocation motion, and resulted in higher creep resistance compared to the base alloy and Ti/V-containing alloys, which is generally in agreement with the results of creep tests (Section 3.3).

However, the Ti/V-containing alloys (V, TiV, Ti, and TiZr) exhibited a higher minimum creep rate than the base alloy (Fig. 9a). This phenomenon is another factor that influences the creep resistance, that is, the grain size. The grain boundaries at high temperatures are weak points, as they provide express channels for dislocation movement. In addition, grain boundary sliding often occurs when the grain size is smaller than a certain value, for example, <50 μm [42, 43]. The smaller the grain size, the larger the grain boundary area, and the weaker the inhibition of dislocation motion and grain rotation during creep. The grain sizes of the V, TiV, Ti, and TiZr alloys were much smaller than those of the base alloy (Fig. 2 and Table 2). Although these alloys exhibited lower λ than the base alloy, their small grain size resulted in higher minimum creep rates than that of the base alloy before the base alloy was in the ternary stage (Fig. 9a). Among the four Ti/V-containing alloys, the TiZr alloy had the lowest λ and the highest minimum creep rate owing to its smallest grain size. The same is true for the Zr-containing alloys (ZrV, Zr, and TiZrV). The TiZrV alloy showed a similar λ to the ZrV alloy and a lower λ than the Zr alloy (Fig. 12a); however, its grain size was 3-5 times smaller than that of the Zr and ZrV alloys (Table 2). The results of the creep tests showed that the minimum creep rate of the TiZrV alloy was higher and the corresponding creep resistance was lower than those of the two alloys (Fig. 9a).

4.3 Comparison of the overall performance at elevated temperature for different alloys

It is apparent that the Zr-containing alloys exhibited excellent elevated-temperature YS and superior creep resistance. However, the poisonous effect of Zr addition in both Zr and ZrV alloys on grain refinement caused a very coarse grain structure. The grain sizes of the ZrV and Zr alloys reached 124 and 194 μm, respectively, which were several times higher than those of the other TE-containing alloys (Table 2). In general, Al-Cu cast alloys are highly susceptible to hot tearing during solidification and casting [44]. The coarse grain structure causes severe hot tearing and reduces castability, which limits the application of Al-Cu cast alloys [45]. Numerous studies have shown that a fine equiaxed grain structure in cast aluminum alloys can significantly reduce the susceptibility to hot tearing [45-47]. In the present work, the further addition of Ti as a grain growth restrictor in Zr-containing alloys could compensate for the Zr poisoning effect and effectively refine the grain structure. Instead of a relatively low Ti (0.05 wt%) in Zr and ZrV alloys, the TiZrV alloy contained 0.17 wt% Ti, resulting in a much finer grain size of 39 μm, which is expected to have a low susceptibility to hot tearing.

To compare the overall performance at elevated temperatures for all the experimental alloys, a schematic chart is illustrated in Fig. 15 based on the three factors (YS, creep resistance, and grain structure) and their ranking discussed above. It can be seen that both ZrV and TiZrV alloys achieved excellent YS and creep resistance, but the ZrV alloy had the worst coarse grain structure. In terms of the comprehensive properties — excellent elevated-temperature YS, superior creep resistance, and fine grain structure — the TiZrV alloy outperformed the eight experimental alloys studied and could be considered the first choice from an industrial and engineering standpoint.

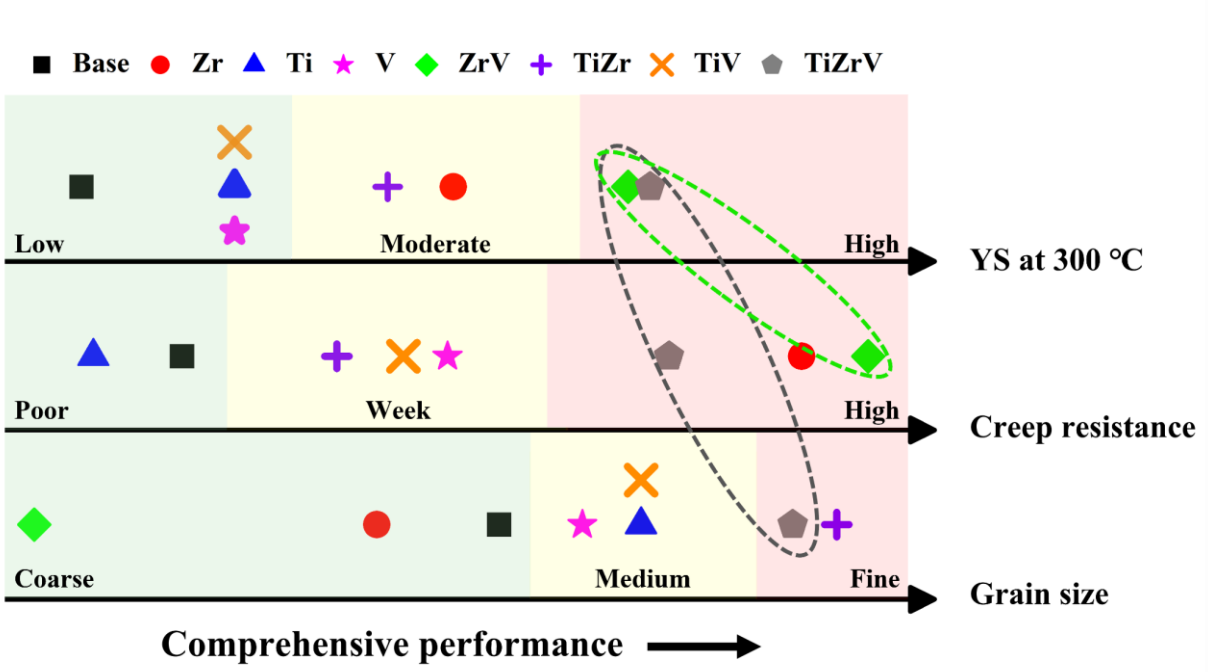

Fig. 15 The comprehensive elevated-temperature performance of all the experimental alloys.

5. Conclusions

1) The addition of three transition elements (Zr, Ti, and V) significantly increased the coarsening resistance of θ′ precipitates during thermal exposure at 300 ℃ (T7A state) and further creep deformation, resulting in finer and more densely distributed θ′ relative to the base alloy. When the TEs were individually added, Zr addition showed the best efficiency for stabilizing θ′. The efficiency was enhanced by the combined addition of TEs, and the combination of Zr + V and Ti + Zr + V yielded the highest efficiency.
2) The addition of TEs considerably improves the yield strength at both room temperature and 300 ℃. When added individually, Zr addition was more effective than Ti or V addition. With combined additions, both ZrV and TiZrV alloys achieved the highest YS at 300 ℃ after T7A. A close relationship between YS and the distribution and thermal stability of the θ′ precipitates was observed.
3) The creep resistance at elevated temperatures was affected by the thermal stability of θ′ and grain size of the Al-Cu 224 alloys. The Zr-containing alloys (ZrV, Zr, and TiZrV) exhibited superior creep resistance owing to the excellent thermal stability of θ′, whereas the Ti/V-

containing alloys (Ti, V, TiV, and TiZr) had a negative effect on the creep resistance due to their small grain size.

4) To avoid the coarse grain structure and reduce the susceptibility to hot tearing, the combined addition of the TiZrV alloy exhibited the optimum elevated-temperature performance and would be the best choice among the eight experimental alloys studied.

Acknowledgement

The authors would like to acknowledge the financial support of the Natural Sciences and Engineering Research Council of Canada (NSERC) under the Grant No. CRDPJ 514651-17 and Rio Tinto Aluminum through the Research Chair in the Metallurgy of Aluminum Transformation at the University of Quebec in Chicoutimi.

References

[1] M. Javidani, D. Larouche, Application of cast Al–Si alloys in internal combustion engine components, Int. Mater. Rev. 59.3 (2014) 132-158. https://doi.org/10.1179/1743280413Y.0000000027

[2] M. Garat, J.F. Major, D. Jean, Copper aluminum alloy molded part having high mechanical strength and hot creep resistance, 2012, U.S. Patent App. No. 13/516,799.

[3] A. Shyam, Y. Yamamoto, D. Shin, S. Roy, J.A. Haynes, P.J. Maziasz, A. Sabau, A.F. Rodriguez-Jasso, J.A. Gonzalez-Villarreal, J. Talamantes-Silva, L. Zhang, C.R. Glaspie, S. Mirmiran, Aluminum alloy compositions and methods of making and using the same. 2017, US Patent App. 15/160,926.

[4] A. Guinier, Heterogeneities in solid solutions, Solid State Phys., Academic Press 9 (1959) 293-398. https://doi.org/10.1016/S0081-1947(08)60568-8

[5] V.A. Phillips, High resolution electron microscope observations on precipitation in Al-3.0% Cu alloy, Acta Metall. 23.6 (1975) 751-767. https://doi.org/10.1016/0001-6160(75)90058-9

[6] A.W. Zhu, E.A. Starke, Stress aging of Al–xCu alloys: experiments, Acta mater. 49.12 (2001) 2285-2295. https://doi.org/10.1016/S1359-6454(01)00119-7

[7] T. Nakajima, M. Takeda, T. Endo, Accelerated coarsening of precipitates in crept Al–Cu alloys, Mater. Sci. Eng. A 387 (2004) 670-673. https://doi.org/10.1016/j.msea.2004.01.131

[8] S. Roy, L.F. Allard, A. Rodriguez, W.D. Porter, A. Shyam, Comparative evaluation of cast aluminum alloys for automotive cylinder heads: Part II—mechanical and thermal properties, Metall. Mater. Trans. A 48.5 (2017) 2543-2562. https://doi.org/10.1007/s11661-017-3986-0
[9] A. Shyam, S. Roy, D. Shin, J.D. Poplawsky, L.F. Allard, Y. Yamamoto, J.R. Morris, B. Mazumder, J.C. Idrobo, A. Rodriguez, T.R. Watkins, J.A. Haynes, Elevated temperature microstructural stability in cast AlCuMnZr alloys through solute segregation, Mater. Sci. Eng. A 765 (2019): 138279. https://doi.org/10.1016/j.msea.2019.138279
[10] J. Rakhmonov, K. Liu, L. Pan, F. Breton, X.G. Chen, Enhanced mechanical properties of high-temperature-resistant Al–Cu cast alloy by microalloying with Mg, J. Alloys Compd. 827 (2020): 154305. https://doi.org/10.1016/j.jallcom.2020.154305
[11] D. Li, K. Liu, J. Rakhmonov, X.G. Chen, Enhanced thermal stability of precipitates and elevated-temperature properties via microalloying with transition metals (Zr, V and Sc) in Al–Cu 224 cast alloys, Mater. Sci. Eng. A 827 (2021): 142090. https://doi.org/10.1016/j.msea.2021.142090
[12] Y. H. Gao, L.F. Cao, C. Yang, J.Y. Zhang, G. Liu, J. Sun, Co-stabilization of θ′-Al2Cu and Al3Sc precipitates in Sc-microalloyed Al–Cu alloy with enhanced creep resistance, Mater. Today Nano 6 (2019): 100035. https://doi.org/10.1016/j.mtnano.2019.100035
[13] B. Rouxel, M. Ramajayam, T.J. Langan, J. Lamb, P. G. Sanders, T. Dorin, Effect of dislocations, Al3 (Sc, Zr) distribution and ageing temperature on θ′ precipitation in Al-Cu-(Sc)-(Zr) alloys, Mater. 9 (2020): 100610. https://doi.org/10.1016/j.mtla.2020.100610
[14] Y.H. Gao, L.F. Cao, J. Kuang, J.Y. Zhang, G. Liu, J. Sun, Assembling dual precipitates to improve high-temperature resistance of multi-microalloyed Al–Cu alloys, J. Alloys Compd. 822 (2020): 153629. https://doi.org/10.1016/j.jallcom.2019.153629
[15] B.A. Chen, G. Liu, R.H. Wang, J.Y. Zhang, L. Jiang, J.J. Song, J. Sun, Effect of interfacial solute segregation on ductile fracture of Al–Cu–Sc alloys, Acta mater. 61.5 (2013) 1676-1690. https://doi.org/10.1016/j.actamat.2012.11.043
[16] C. Yang, P. Zhang, D. Shao, R.H. Wang, L.F. Cao, J.Y. Zhang, G. Liu, B.A. Chen, J. Sun, The influence of Sc solute partitioning on the microalloying effect and mechanical properties of Al-Cu alloys with minor Sc addition, Acta Mater. 119 (2016) 68-79. https://doi.org/10.1016/j.actamat.2016.08.013

[17] D. Shin, A. Shyam, S. Lee, Y. Yamamoto, J.A. Haynes, Solute segregation at the Al/θ′-Al2Cu interface in Al-Cu alloys, Acta Mater. 141 (2017) 327-340. https://doi.org/10.1016/j.actamat.2017.09.020

[18] J. D. Poplawsky, B.K. Milligan, L.F. Allard, D. Shin, P. Shower, M.F. Chisholm, A. Shyam, The synergistic role of Mn and Zr/Ti in producing θ′/L12 co-precipitates in Al-Cu alloys, Acta Mater. 194 (2020) 577-586. https://doi.org/10.1016/j.actamat.2020.05.043

[19] K.E. Knipling, D.C. Dunand, D.N. Seidman, Criteria for developing castable, creep-resistant aluminum-based alloys–A review, Int. J. Mater. Res. 97.3 (2006) 246-265. https://doi.org/10.3139/ijmr-2006-0042

[20] B.K. Milligan, S. Roy, C.S. Hawkins, L.F. Allard, A. Shyam, Impact of microstructural stability on the creep behavior of cast Al–Cu alloys, Mater. Sci. Eng. A 772 (2020): 138697. https://doi.org/10.1016/j.msea.2019.138697

[21] J.U. Rakhmonov, S. Bahl, A. Shyam, D.C. Dunanda, Cavitation-resistant intergranular precipitates enhance creep performance of θ′-strengthened Al-Cu based alloys, Acta Mater. (2022): 117788. https://doi.org/10.1016/j.actamat.2022.117788

[22] S. Mondol, S. Kashyap, S. Kumar, K. Chattopadhyay, Improvement of high temperature strength of 2219 alloy by Sc and Zr addition through a novel three-stage heat treatment route, Mater. Sci. Eng. A 732 (2018) 157-166. https://doi.org/10.1016/j.msea.2018.07.003

[23] Y.H. Gao, C. Yang, J.Y. Zhang, L.F. Cao, G. Liu, J. Sun, Stabilizing nanoprecipitates in Al-Cu alloys for creep resistance at 300 °C, Mater. Res. Lett. 7.1 (2019) 18-25. https://doi.org/10.1080/21663831.2018.1546773

[24] Z.C. Sims, O.R. Rios, D. Weiss, P.E.A. Turchi, A. Perron, J.R.I. Lee, T.T. Li, J.A. Hammons, M. Bagge-Hansen, T.M. Willey, K. An, Y. Chen, A.H. King, S.K. McCall, High performance aluminum–cerium alloys for high-temperature applications, Mater. Horiz. 4.6 (2017) 1070-1078. https://doi.org/10.1039/C7MH00391A

[25] S.K. Makineni, S. Sugathan, S. Meher, R. Banerjee, S. Bhattacharya, S. Kumar, K. Chattopadhyay, Enhancing elevated temperature strength of copper containing aluminium alloys by forming L12 Al3Zr precipitates and nucleating θ″ precipitates on them, Sci. Rep. 7.1 (2017) 1-9. https://doi.org/10.1038/s41598-017-11540-2

[26] P. Hu, K. Liu, L. Pan, X.G. Chen, Effect of Mg microalloying on elevated-temperature creep resistance of Al–Cu 224 cast alloys, Mater. Sci. Eng. A 851 (2022): 143649. https://doi.org/10.1016/j.msea.2022.143649

[27] J.F. Nie, B.C. Muddle, Strengthening of an Al–Cu–Sn alloy by deformation-resistant precipitate plates, Acta Mater. 56 (2008) 3490-3501. https://doi.org/10.1016/j.actamat.2008.03.028

[28] J. Li, F.S. Hage, Q.M. Ramasse, P. Schumacher, The nucleation sequence of α-Al on TiB2 particles in Al-Cu alloys, Acta Mater. 206 (2021): 116652. https://doi.org/10.1016/j.actamat.2021.116652

[29] B.S. Murty, S.A. Kori, M. Chakraborty, Grain refinement of aluminium and its alloys by heterogeneous nucleation and alloying, Int. Mater. Rev. 47.1 (2002) 3-29. https://doi.org/10.1179/095066001225001049

[30] D. Qiu, J.A. Taylor, M.-X. Zhang, Understanding the co-poisoning effect of Zr and Ti on the grain refinement of cast aluminum alloys, Metall. Mater. Trans. A 41.13 (2010) 3412-3421. https://doi.org/10.1007/s11661-010-0404-2

[31] C. Wolverton, Solute–vacancy binding in aluminum, Acta Mater. 55.17 (2007) 5867-5872. https://doi.org/10.1016/j.actamat.2007.06.039

[32] J. Peng, S. Bahl, A. Shyam, J.A. Haynes, D. Shin, Solute-vacancy clustering in aluminum, Acta Mater. 196 (2020) 747-758. https://doi.org/10.1016/j.actamat.2020.06.062

[33] S. Mondol, S.K. Makineni, S. Kumar, K. Chattopadhyay, Enhancement of high temperature strength of 2219 alloys through small additions of Nb and Zr and a novel heat treatment, Metall. Mater. Trans. A 49.7 (2018) 3047-3057. https://doi.org/10.1007/s11661-018-4614-3

[34] K.E. Knipling, D.C. Dunand, D.N. Seidman, Precipitation evolution in Al–Zr and Al–Zr–Ti alloys during isothermal aging at 375–425 ℃, Acta Mater. 56.1 (2008) 114-127. https://doi.org/10.1016/j.actamat.2007.09.004

[35] Z. Shen, Q. Ding, C. Liu, J. Wang, H. Tian, J. Li, Z. Zhang, Atomic-scale mechanism of the θ″→ θ′ phase transformation in Al-Cu alloys, J. Mater. Sci. Technol. 33.10 (2017) 1159-1164. https://doi.org/10.1016/j.jmst.2016.08.031

[36] L. Jin, K. Liu, X.G. Chen, Evolution of dispersoids and their effects on elevated-temperature strength and creep resistance in Al-Si-Cu 319 cast alloys with Mn and Mo additions, Mater. Sci. Eng. A 770 (2020): 138554. https://doi.org/10.1016/j.msea.2019.138554

[37] D. Yao, W. Zhao, H. Zhao, F. Qiu, Q. Jiang, High creep resistance behavior of the casting Al–Cu alloy modified by La, Scripta Mater. 61 (2009) 1153-1155. https://doi.org/10.1016/j.scriptamat.2009.09.007
[38] M.E. Kassner, Fundamentals of creep in metals and alloys, Butterworth-Heinemann, 2015.
[39] Y. Xu, L. Zhan, L. Xu, M. Huang, Experimental research on creep aging behavior of Al-Cu-Mg alloy with tensile and compressive stresses, Mater. Sci. Eng. A 682 (2017) 54-62. https://doi.org/10.1016/j.msea.2016.11.043
[40] C. Yang, L. Cao, Y. Gao, P. Cheng, P. Zhang, J. Kuang, J. Zhang, J. Sun, Nanostructural Sc-based hierarchy to improve the creep resistance of Al–Cu alloys, Mater. Des. 186 (2020): 108309. https://doi.org/10.1016/j.matdes.2019.108309
[41] W.S. Tian, Q.L. Zhao, Q.Q. Zhang, F. Qiu, Q.C. Jiang, Superior creep resistance of 0.3 wt% nano-sized TiCp/Al-Cu composite, Mater. Sci. Eng. A 700 (2017) 42-48. https://doi.org/10.1016/j.msea.2017.05.101
[42] O.D. Sherby, E.M. Taleff, Influence of grain size, solute atoms and second-phase particles on creep behavior of polycrystalline solids, Mater. Sci. Eng. A 322.1-2 (2002) 89-99. https://doi.org/10.1016/S0921-5093(01)01121-2
[43] K.R. Athul, U.T.S. Pillai, A. Srinivasan, B.C. Pai, A review of different creep mechanisms in Mg alloys based on stress exponent and activation energy, Adv. Eng. Mater. 18.5 (2016) 770-794. https://doi.org/10.1002/adem.201500393
[44] H.K. Kamga, D. Larouche, M. Bournane, A. Rahem, Hot tearing of aluminum–copper B206 alloys with iron and silicon additions, Mater. Sci. Eng. A 527.27-28 (2010) 7413-7423. https://doi.org/10.1016/j.msea.2010.08.025
[45] S. Li, K. Sadayappan, D. Apelian, Role of grain refinement in the hot tearing of cast Al-Cu alloy, Metall. Mater. Trans. B 44.3 (2013) 614-623. https://doi.org/10.1007/s11663-013-9801-4
[46] M. Easton, H. Wang, J. Grandfield, D. StJohn, E. Sweet, An analysis of the effect of grain refinement on the hot tearing of aluminium alloys, Mater. forum. 28 (2004) 224-229
[47] M. Easton, J.F. Grandfield, D.H. StJohn, B. Rinderer, The effect of grain refinement and cooling rate on the hot tearing of wrought aluminium alloys, Mater. Sci. forum. Trans Tech Publications Ltd, 519 (2006) 1675-1680. https://doi.org/10.4028/www.scientific.net/MSF.519-521.1675